Fusion of SAR and Optical Image for Sea Ice Extraction

LI Wanwu[1], LIU Lin[1], [*], and ZHANG Jixian[2]

1) *College of Geodesy and Geomatics, Shandong University of Science and Technology, Qingdao* 266590, *China*
2) *National Quality Inspection and Testing Center for Surveying and Mapping Products, Beijing* 100830, *China*

Abstract It is difficult to balance local details and global distribution using a single source image in marine target detection of a large scene. To solve this problem, a technique based on the fusion of optical image and synthetic aperture radar (SAR) image for the extraction of sea ice is proposed in this paper. The Band 2 (B2) image of Sentinel-2 (S2) in the research area is selected as optical image data. Preprocessing on the optical image, such as resampling, projection transformation and format conversion, are conducted to the S2 dataset before fusion. Imaging characteristics of the sea ice have been analyzed, and a new deep learning (DL) model, OceanTDL5, is built to detect sea ices. The fusion of the Sentinel-1 (S1) and S2 images is realized by solving the optimal pixel values based on deriving Poisson Equation. The experimental results indicate that the use of a fused image improves the accuracy of sea ice detection compared with the use of a single data source. The fused image has richer spatial details and a clearer texture compared with the original optical image, and its material sense and color are more abundant.

Key words sea ice detection; image fusion; SAR image; optical image; Poisson Equation

1 Introduction

The occurrence of sea ice may cause port freezing and tunnel blocking, even affect marine fisheries. Therefore, the detection and extraction of sea ice are extremely important. The existing researches on marine target detection are mainly focused on ships, *e.g.*, ship target detection based on synthetic aperture radar (SAR) images (Hwang *et al.*, 2017; Iervolino and Guida, 2017; Hwang and Jung, 2018; Cui *et al.*, 2019) and optical images (Chen and Gong, 2010; Zhu *et al.*, 2010; Wang *et al.*, 2011; Mattyus, 2013; Ren, 2016; Ji *et al.*, 2017; Nie *et al.*, 2017; Heiselberg, 2019).

Spaceborne SAR (synthetic aperture radar) has been proven to be an effective tool for monitoring sea ice (Ressel *et al.*, 2016; Miguel *et al.*, 2017), and over the years, sea ice detection technique based on SAR images has been significantly improved. Herzfeld *et al.* (2016) applied geostatistical methods to automatically classify sea ice by using SAR data. Ressel and Singha (2016) compared the polarimetric backscatter characteristics of sea ice in spaceborne X and C band SAR images and proposed a supervised classification algorithm for sea ice. Fang *et al.* (2007) proposed a multiclass classification method for a large area glacier by using spaceborne single-polarimetric SAR intensity image. They also constructed a linear classifier

with the supervised neighborhood embedding *via* sparse characteristic representation (Fang *et al.*, 2017). Lohse *et al.* (2019) proposed a numerically optimized decision-tree algorithm, which was applied in the classification of sea ice using SAR data. Xie *et al.* (2020) proposed a method for differentiating seawater from sea ice by using quad-polarized C band SAR image. Johansson *et al.* (2020) investigated a method for identifying oil slick and sea ice by using SAR image. Park *et al.* (2016) proposed a classification algorithm for sea ice in Sentinel-1 (S1) image based on a machine learning model.

To compensate for the deficiency of SAR image, which is difficult to be interpreted, some scholars use multispectral images to classify and detect sea ice (Han *et al.*, 2016; Heiselberg and Heiselberg, 2017; Su *et al.*, 2019; MacGregor *et al.*, 2020). Typically, Barbieux *et al.* (2018) proposed an algorithm to distinguish the ice from open water on ice lakes by using multispectral data obtained from Landsat 8. This algorithm has a significantly high optimal threshold stability, which can better separate the ice/water mixture from the ground. Han *et al.* (2018) proposed a classification framework for the detection of sea ice, which combines active learning (AL) and semi-supervised learning (SSL), by using transductive support vector machine to classify high spectral and multispectral images.

The fusion of SAR and optical images in the existing researches is mainly applied in land classification (Liu *et al.*, 2017; Sukawattanavijit *et al.*, 2017; Aswatha *et al.*, 2020). To exploit the advantages of SAR and multispectral data, some scholars adopt the fusion of SAR and mul-

---

* Corresponding author. Tel: 0086-532-80681183
  E-mail: liulin2009@126.com

tispectral images to marine target detection (Park *et al.*, 2018). Vijay and Gopalan (2012) used the images captured by TerraSAR-X and Indian Remote Sensing Satellite to analyze the glacial characteristics in the Himalayas by using the IHS (intensity, hue, saturation) fusion technology and Principal Component Analysis (PCA) based technology. Shah *et al.* (2019) employed the pixel-based technology to fuse the images captured by Radar Imaging Satellite-1 and RESOURCESAT-2. Compared with the original multispectral and SAR images, the fusion image provides an improved recognition of characteristics, such as blue ice and lake ice. Yu *et al.* (2019) proposed a new sea ice classification framework based on locality, which classifies the pixels of the fused image by using a sliding integration strategy and retains the local characteristic of the source image in both the spatial and characteristic domains. Heiselberg (2020) optimized a convolutional neural network with a series of hyperparameters and used S1 (Sentinel-1) SAR and S2 (Sentinel-2) multispectral images in the experiments to achieve an improved ship and iceberg classification accuracy.

In general, the fusion of SAR and multispectral images is mainly applied in land classification and less in marine target detection. In the field of marine target detection, numerous researches focus more on ships detection and less on sea ice detection. Moreover, for sea ice detection, most works mainly adopt SAR or optical image as single data source. Also, the fus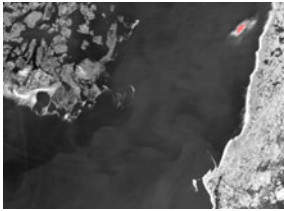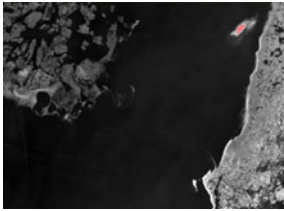ion of SAR and optical images is rarely used for the detection and extraction of sea ice. Thus, in this paper, such a fusion image is employed, and the spectral color and interpretation characteristics of multispectral images are exploited to compensate for the deficiencies of SAR image and improve the accuracy of sea ice detection.

2 Data

2.1 Image Data Selection

S2 Multispectral Instrument (MSI) data were obtained at three resolutions: 10-m resolution, which includes four bands; 20-m resolution, which includes six bands, four (705, 740, 783, and 865 nm) of which are used for vegetation characteristics and two larger SWIR (Short Wave Infra-Red) bands (1610 and 2190 nm) for snow/ice/cloud detection or vegetation moisture assessment; and 60-m resolution, which includes three bands that are mainly used for cloud shielding and atmospheric correction. The S2 image with 10-m resolution was selected, and the example of each band is shown in Table 1. In Band 4 (B4), the clouds and fog are clearly visible. In Band 3 (B3), they are faintly visible. In Band 8 (B8) and B2 (Band 2), the clouds and fog cannot be seen. But in B2 the image shows a better saturation and stronger penetration, thus better comprehensive effect. Therefore, the B2 band data of S2 with 10-m resolution was utilized to fuse with the previously processed S1 SAR dataset for sea ice detection.

Table 1 Example images in four band of S2 with 10-m resolution

Band and resolution	Image of drilling platform	Image of sea ice
B2 10 m		
B3 10 m		
B4 10 m		
B8 10 m		

2.2 Image Preprocessing

The SAR datasets for sea ice detection were collected by S1 on February 9, 2016, with a file name of S1A_IW_ SLC_1SDV_20160209T215542_20160209T215609_009 875_00E783_83E7.SAFE. For the fusion of optical image and SAR image, multispectral image data collected by S2 on February 7, 2016, are used, with the file names of S2A_OPER_PRD_MSIL1C_PDMC_20160207T114115_ R132_V20160207T025602_20160207T025602.SAFE and S2A_OPER_PRD_MSIL1C_PDMC_20160207T113337_ R132_V20160207T025602_20160207T025602.SAFE. The S2 image is preprocessed according to the procedure shown in Fig.1.
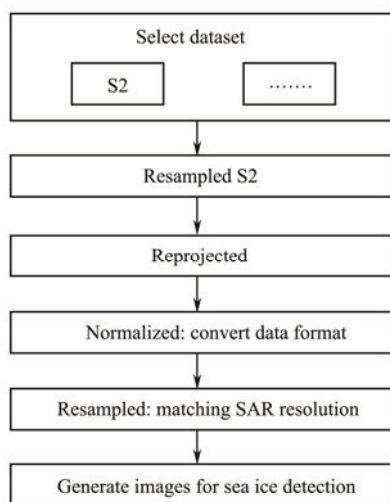
is shown in Fig.4.

Fig.2 Resampling results.

Fig.1 S2 image preprocessing procedure.

The research area is in the Bohai Sea. The level-1C multi-resolutions products in the north of the 51°N in the S2 image were resampled and converted into 10-m single-resolution data, thus obtaining a 30978×30978 pixel image. The nearest-neighbor method is used to interpolate the pixel values of the image, and the nearest is selected. To improve the imaging speed, the pyramid level was selected for resampling, and the resulting image is shown in Fig.2. To improve the accuracy of sea ice detection, the opaque clouds and cirrocumulus in level-1C products were extracted in the S2 image of the research area, which are colored in red in Fig.2. To improve the efficiency of sea ice detection, the land in the research area needs to be removed by setting the pixels to be null values and only the marine area was extracted. The extracted S2 image of the marine research area is shown in Fig.3.

To facilitate the fusion of S1 and S2 images for sea ice detection, the two images need to be projected to the same geographic reference system. The extracted S2 image of the marine research area was resampled by using the nearest-neighbor, bilinear, and bicubic interpolations.

To ensure the timeliness of target detection, the nearest-neighbor interpolation is employed to reproject the S2 image in this work. Only the S2 image in the overlapped area with the SAR image was reprojected, and the result

Fig.3 The extracted image in marine research area.

Fig.4 S2 image in the research area after reprojection.

2.3 Image Characteristics Analysis of Sea Ice

After preprocessing, the multispectral image data with 14-m resolution, consistent with the SAR image data, were obtained *via* resampling in the study area. Statistical analysis of the image characteristics of the sea ice in the research area is performed on a small number of samples and results are shown in Fig.5. The total number of pixels included in the statistical analysis is 12821093, and the
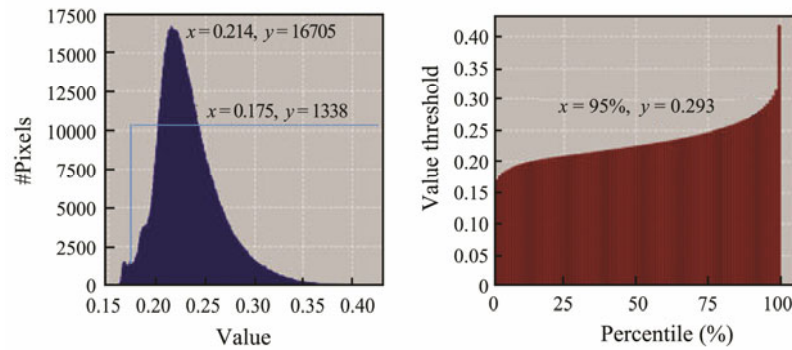
Fig.5 Statistical characteristics of sea ice.

pixel characteristic value is shown in Table 2.

Table 2 Pixel characteristic value of sea ice

Index	Value
Minimum	0.15850
Maximum	0.41879
Mean	0.23188
Sigma	0.03184
Median	0.22617
Coef variation	0.28819
ENL	12.03990
P75 threshold	0.24804
P80 threshold	0.25481
P85 threshold	0.26314
P90 threshold	0.27459
Max error	0.00026

The image characteristics of the overall marine research area are analyzed and the results are shown in Fig.6. The total number of pixels included in the statistical analysis is 133016388, and the pixel characteristic value is shown in Table 3.

Table 3 Pixel characteristic value of marine research area

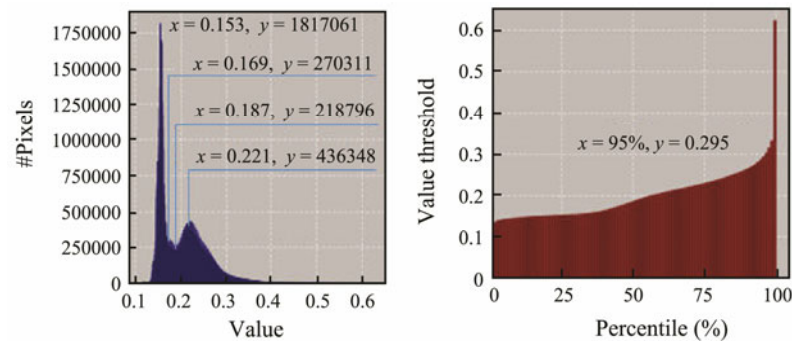| Index	Value
Minimum	0.10859
Maximum	0.62470
Mean	0.20090
Sigma	0.05202
Median	0.19034
Coef variation	0.56681
ENL	3.11255
P75 threshold	0.23298
P80 threshold	0.24226
P85 threshold	0.25414
P90 threshold	0.26859
Max error	0.00051

Fig.6 Statistical characteristics of image in the marine research area.

To obtain the characteristic value of various targets in the research area, the characteristics of the preprocessed image are statistically analyzed, as shown in Table 4.

Table 4 The spectral characteristic value of each target in the research area

Characteristic index	Overall marine area	Sea water	Sea ice
Minimum	0.10859	0.14440	0.15850
Maximum	0.62470	0.16709	0.41879
Average	0.20090	0.15560	0.23188

The statistical histogram of the overall marine research area exhibited multiple peaks, and sea ice exhibited a single peak. The area with an average value of 0.22296 is determined to be sea ice. Moreover, when a small number of sea ice samples were analyzed, a peak with the small reflection value of near 0.17 appeared, as well as for the overall marine research area. It is preliminarily determined that the region with this characteristic value is covered by semi-dissolved sea ice or sea ice covered by thin sea water. It is also found that the research area, where the reflection value is over 0.3 (5% of the total image), is mostly covered by coastal sea ice and a small part sea ice in the marine, not drilling platforms and coastal embankments, which is different from that shown by the SAR image. The comparison of the various targets between the S1 and S2 images is shown in Fig.7.
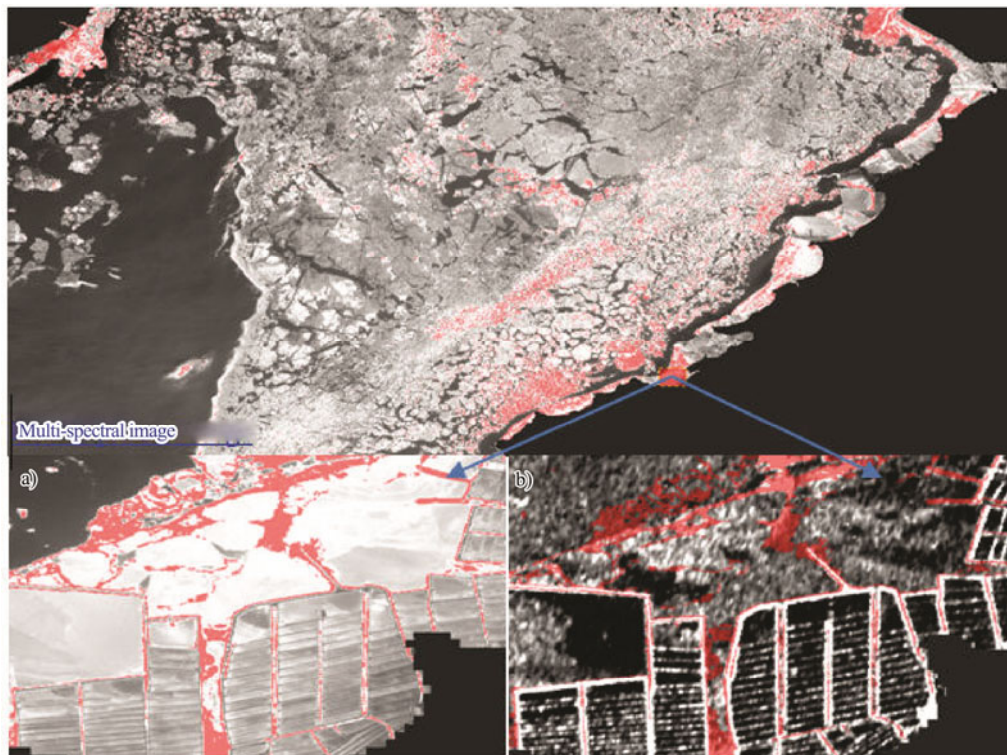
Fig.7 Target comparison of the S1 and S2 images. a), the background is multispectral image. The dyke is gray. b), the background is SAR image. The dyke is white.

2.4 Detection Dataset Construction

The integral data of [0, 255] after linear scaling conversion were resampled according to 14-m resolution to construct the dataset of S2 for marine target detection. The S2 dataset constructed for marine target detection includes a total of 48984320 pixels, which provides training, testing and verification dataset for the neural network to learn the sea ice detection. Fig.8 shows the research area and statistical characteristics of sea water and sea ice. The areas numbers 1–12 in the figure are sea water, which consists of 20521200 pixels, including 26175 28×28 pixels. The areas numbered 13–28 in the figure are covered by sea ice with 28463120 pixels, including 36305 28×28 pixels. As can be seen from Fig.8, there are two peaks appear for sea ice. The single peak with a pixel value between 33 and 39 is mainly caused by semi-melting sea ice or sea ice covered by sea water, as indicated in red in the enlarged image No. 17.

3 Method

Fusion of remote sensing images is performed by processing redundant or complementary multisource remote sensing data in space, spectrum, and time according to certain rules or algorithms. The composite image data with new spatial, spectrum, and time characteristics generally have more accurate and richer information compared with any single data. In this paper, the method of solving the optimal pixel value based on constructing Poisson Equation is used to fuse images, which can well retain the gra-

dient information of the source image and fusion the background information of the source image and target image.

3.1 DL Based Initial Detection

3.1.1 OceanTDL5 construction

A deep learning model OceanTDL5 for sea ice detection was constructed. It is composed of 1 Layer, 1 Group and 1 fully connected Dense (Fig.9). The organization form of the Layer is W*X_pluse_b-relu-Dropout-reshape. The middle Group includes 3 layers, and its organization form is as (W*X_pluse_b-relu-Dropout-reshape)*3. The organization form of fully connected Dense Layer is W*X_pluse_b-relu. The characteristic information is gradually reduced through 529-121-25-9 from 784 that were input at the beginning. Finally, a full connection containing 9 neurons is used to perform weighted summation and Relu activate to compress to 2 characteristics, which are input to Softmax of Loss Layer for classification.

3.1.2 Sea ice initial detection

The sea ice is initially detected from the S1 and S2 images individually by using the OceanTDL5 model and three methods including StErf (Standard Error function) method, Loglogistic distribution method, and Sgmloglog method that is proposed by the authors previously to extract targets. Then the results were stored as marine target database tags_idlab.db and image_idDate.db for S1 and S2. Before the image fusion, preliminary data processing is carried out as the following procedure (Fig.10).
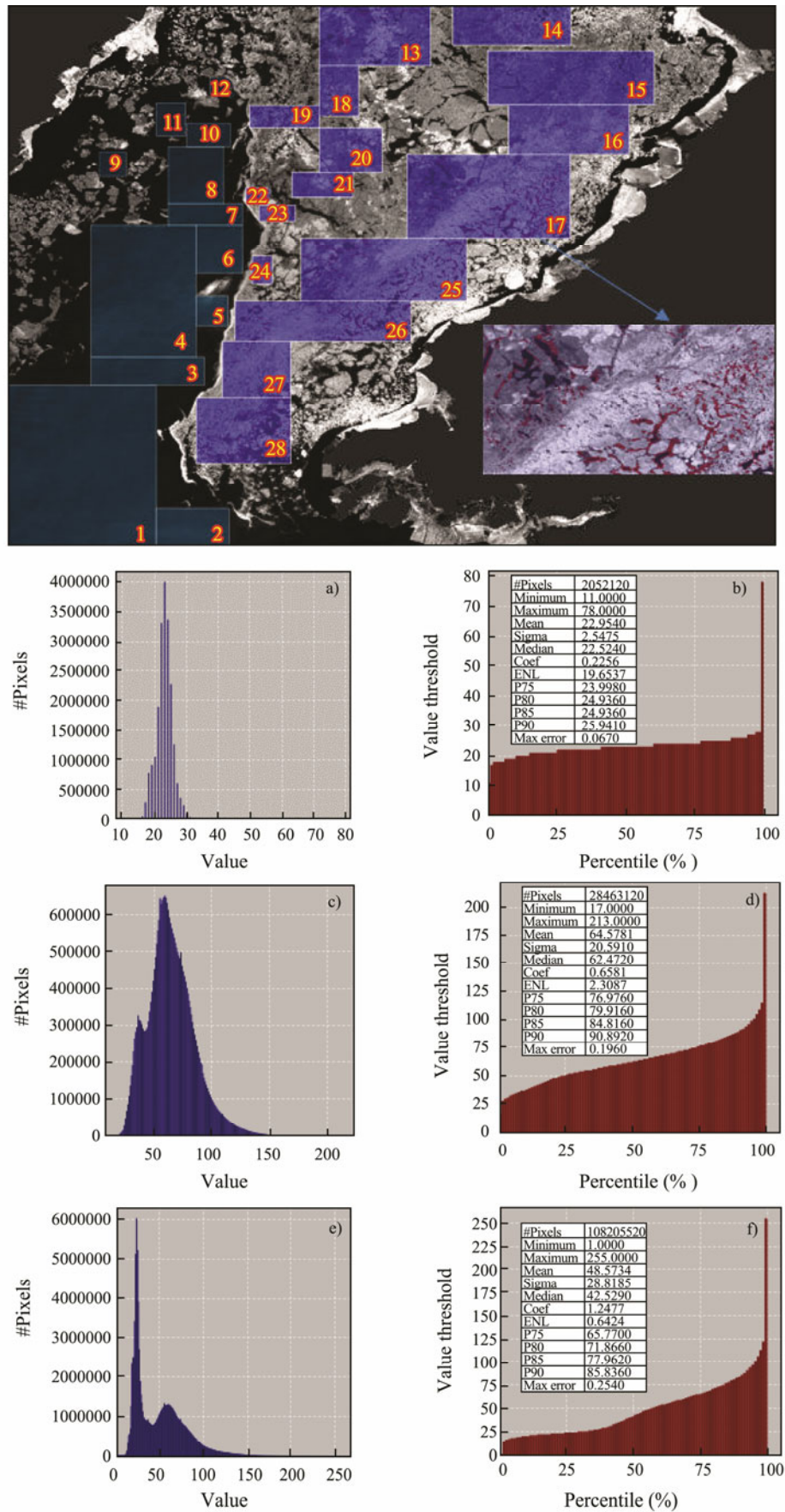
Fig.8 Sea ice detection dataset with 14-m resolution. a) and b) for sea water; c) and d) for sea ice; e) and f) for overall marine research area.
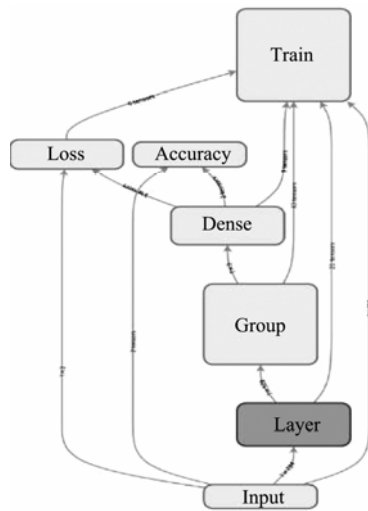
Fig.9 OceanTDL5.

3.2 Image Fusion Based Detection

3.2.1 Fusion method

By solving the optimal pixel values from the Poisson Equation, the image pixels in the fusion area can be reconstructed. The algorithm is shown in Fig.11.

Poisson Equation is expressed as follows:

$$\Delta f = \mathrm{div}(\nabla u) = \mathrm{div}(\frac{\partial f}{\partial x} i, \frac{\partial f}{\partial y} j) = \frac{\partial^2 f}{\partial x^2} + \frac{\partial^2 f}{\partial y^2}. \quad (1)$$

The iterative method is employed for the discrete computation of Eq. (1). By convoluting with Laplace convolution kernel, the divergence image of the image u to be fused can be solved, in which Laplacian convolution kernel takes the following form:
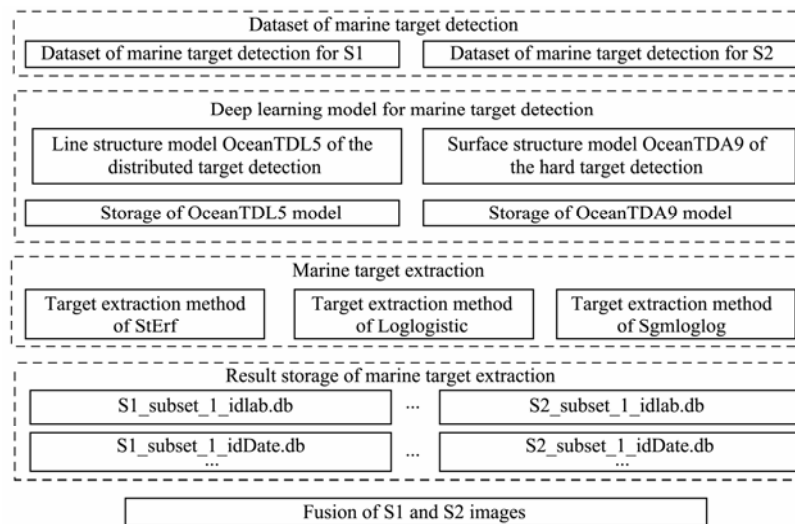

Fig.10 Data process flow before image fusion.

$$k = \begin{bmatrix} 0 & 1 & 0 \\ 1 & -4 & 1 \\ 0 & 1 & 0 \end{bmatrix}. \quad (2)$$

The discrete formula of Laplacian operator on the image u to be fused is as follows:

$$\mathrm{div}(\nabla u) = \Delta u = u_{i+1,j} + u_{i,j+1} + u_{i-1,j} + u_{i,j-1} - 4u_{i,j}$$
$$= du_{i,j} = b. \quad (3)$$

The discrete formula of Laplacian operator on the fused image f of the areas covered by the targets is as follows:

$$\Delta f = f_{i+1,j} + f_{i,j+1} + f_{i-1,j} + f_{i,j-1} - 4f_{i,j} = du_{i,j} = \Delta u = b, \quad (4)$$

where

$$f_{i,j} = \frac{1}{4}(f_{i+1,j} + f_{i,j+1} + f_{i-1,j} + f_{i,j-1} - b). \quad (5)$$

In the equation, $du_{i,j}$ is the processed value of the original image u by Laplacian operator previously.

3.2.2 Sea ice detection based on fused images

The initial detection data in ocean target datavase tag_idlab.db and image_idDate.db are used as the data source to fuse the S1 and S2 images for sea ice detection.

1) Calculate the mean difference *meanD* of the pixel values for the suspected targets in the S1 and S2 images.

Read the detection results of the suspected targets in the S1 and S2 images and calculate the mean difference *meanD* of the pixel values.

$$meanD = meanS2 - meanS1 = \frac{\sum Val_{\text{S2-STP}}}{N_{\text{S2-STP}}} - \frac{\sum Val_{\text{S1-STP}}}{N_{\text{S1-STP}}}.$$

$$(6)$$

In the equation, *meanS*1 and *meanS*2 denote the mean pixel value of the suspected targets in the S1 and S2 images, respectively; $Val_{\text{S1–STP}}$ and $Val_{\text{S2–STP}}$ are the pixel values of the suspected targets in the S1 and S2 images, respectively; and $N_{\text{S1–STP}}$, $N_{\text{S2–STP}}$ are the pixel number of

Calculate the gradient field of the image to be fused		Calculate the gradient field of the background image	
Patch_mask_gradX	*Patch_mask_gradY*	*dst_gradX*	*dst_gradY*

Calculate the gradient field of the fused image	
laplacianX = Patch_mask_gradX + dst_gradX	*laplacianY = Patch_mask_gradY + dst_gradY*

Calculate the divergence of the fused image
b = laplacianX + laplacianY

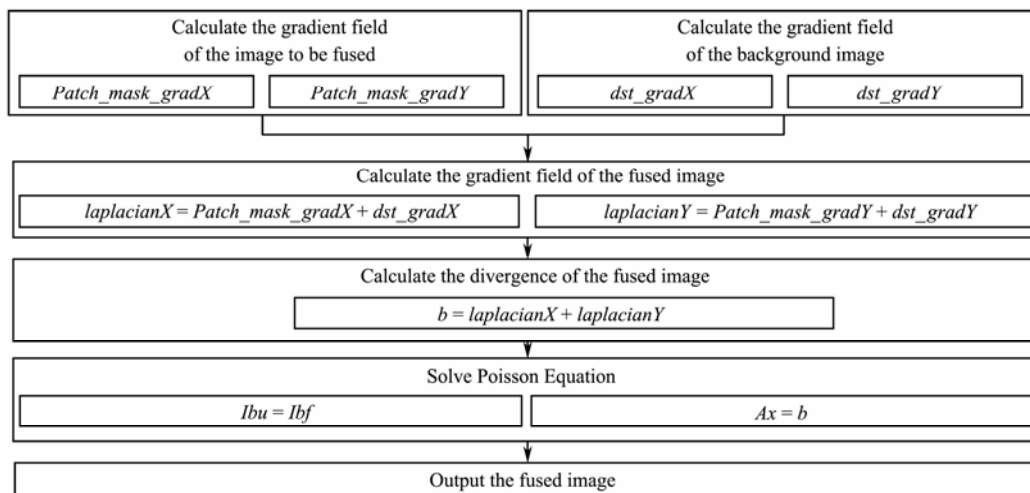| Solve Poisson Equation	
Ibu = Ibf	*Ax = b*

Output the fused image

Fig.11 Algorithm steps of the image fusion.

suspected targets in the S1 and S2 images, respectively.

2) Calculate the pixel values of the suspected targets in the fused image *fusionS*.

The initial pixel values of the fused image (*fusionS*) are calculated as follows:

$$fusionS_{mn} = [Val_{S1\text{-}STP}]_{mn} + meanD . \qquad (7)$$

In the equation, $Val_{S1\text{–}STP}$ denotes the pixel value of the suspected targets in the S1 image, and m and n denote the row and column of the pixels of suspected targets.

3) Calculate the pixel values of the non-distributed targets in the S1 image.

Read the pixel values of non-distributed targets in the S1 image in turn and adjust the pixel values of the 3×3 grid area centered on the target in the S1 image by using the below equation and save them to the array *clusterVal*.

$$clusterVal[j][k] = S1[j][k] + meanD / \varepsilon . \qquad (8)$$

In the equation, j denotes the row number of the S1 image; k is the column number; and ε is the fusion coefficient. According to experimental verification, $\varepsilon=2$ is adopted.

4) Fuse the pixel values of non-distributed targets into the fused image (*fusionS*) of the suspected targets.

The mask image of the image *clusterVal* is established, the center coordinates of the image to be fused are calculated, and the non-distributed target (*clusterVal*) is merged into the suspected target (*fusionS*) image according to the principle of the same boundary pixel value.

4 Experimental Results

The original S1 and S2 images before fusion are shown in Figs.12 and 13, and the fused image obtained according to the method above is shown in Fig.14.

1) Qualitative analysis

In Fig.14, the fused image maintains the spatial details of the SAR image before fusion and the texture sense of

sea ice of the multispectral image, presenting a visual sense of rich color and clear texture. With regard to spectral color, the original SAR image is dark, but the brightness of the fused image is between the SAR and multispectral images. In terms of spatial detail, the fused image is much richer than the original multispectral image and has a strong sense of depth. From the enlarged image (Fig.14), it can be found that the fused image is superior to the SAR image (Fig.12) and the multi-spectral image (Fig.13) in terms of capturing spatial details. From the image interpretation perspective, the fused image is easier to determine the type of marine distribution target than the original SAR image, and is easier to spot the differences between the same types of distribution target than the original multi-spectral image.
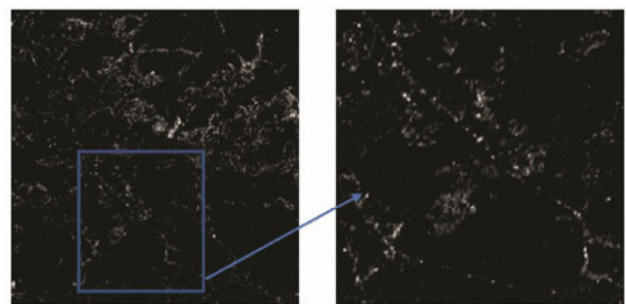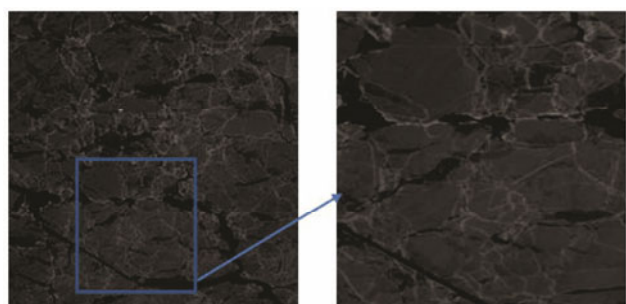

Fig.12 S1 image before fusion.
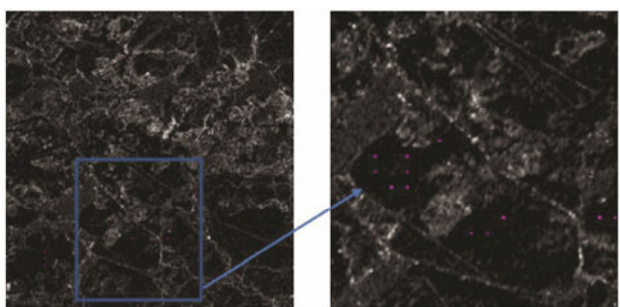

Fig.13 S2 image before fusion.

Fig.14 Fused image of S1 and S2.

2) Quantitative analysis

To evaluate effectiveness of the fusion method, the detection rate index is used to quantitatively analyze the sea ice extracted from the fused image. The sea ice detected using DL models are shown in Fig.15, and the sea ice detected by the fused image of S1 and S2 are shown in Fig.16.

The pink boxes in Fig.15 indicate the area covered by the sea ice detected by the trained OceanTDL5 model. A total of 1804 pieces of sea ice are detected, each containing 28×28 pixels. The detection rate is 96.8%. In Fig.16, the sea ice areas detected by the fusion data of the S1 and S2 images are presented. Table 5 shows the detailed information about the effect of sea ice detection by using the DL model and the fusion data of the S1 and S2 images.

A total of 1861 pieces of sea ice are detected, at a detection rate of 99.7%. The detection accuracy is improved by 3%, the detection time is 3.65 s, and the detection ability of the image with a 14-m resolution is near $67.2 \, \text{km}^2 \text{s}^{-1}$. The undetected sea ice is mainly concentrated in the confluence of sea water and sea ice, where the ice is covered by water or is semi-melted.

Fig.15 Sea ice detected using DL model (pink box).

Table 5 The effect of Sea ice detected using DL model and fusion of the S1 and S2 images

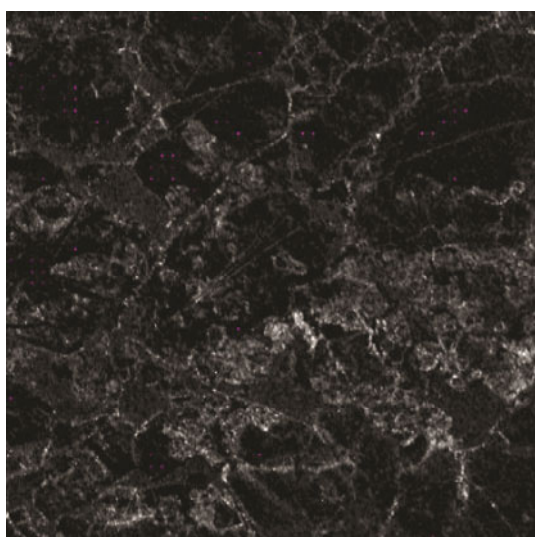| Model	Total number of samples	Sea ice number	Number of detected targets	Number of missed targets	Detection rate	Missing rate	Time consumed (s)	Detection ability ($\text{km}^2 \text{s}^{-1}$)
OceanTDL5	2254	1867	1804	63	96.8%	3.2%	3.17	78.4
Fusion-OceanTDL5	2254	1867	1861	6	99.7%	0.3%	3.65	67.2

Fig.16 Sea ice detected by the fusion of the S1 and S2 images.

5 Conclusions

For the target detection in a large sea area, it is difficult to balance local details and global distribution just by using a single source image because of its intrinsic limitations in imaging. Therefore, in this paper, the SAR images and optical images are fused to extract sea ice in order to take the advantages of the two types of image sources and complement each other.

The fused image maintained the spatial details and clear texture of the SAR image before fusion and the high texture sense (for sea ice) and rich color of the multispectral image. The qualitative analysis reveals that in terms of spatial details, the fused image is richer than the original multispectral image, has a sense of hierarchy, and is superior to the original SAR image and multispectral image in terms of captured spatial details. With regard to the spectral color, the original SAR image is darker, and the brightness of the fused image is between the SAR and multispectral images. From the perspective of image interpretation, the use of the fused image can determine more easily the type of marine distribution target compared with the use of the original SAR image. Moreover, it can determine more easily the difference between the same types of distribution target compared with the original multispectral image.

The detection rate of the sea ice based on the fusion data of the SAR and optical images is 99.7%. The detection accuracy is 3% higher than that of the non-fusion model, and the detection ability for the image with a 14-m resolution is near $67.2 \, \text{km}^2 \text{s}^{-1}$. The undetected sea ice is mainly concentrated in the confluence of sea water and sea

ice, where the ice is covered by water or is semi-melted.

Acknowledgements

References

Aswatha, S. M., Mukherjee, J., Biswas, P. K., and Aikat, S., 2020. Unsupervised classification of land cover using multi-modal data from multi-spectral and hybrid-polarimetric SAR imageries. *International Journal of Remote Sensing*, **41** (14): 5277-5304.

Barbieux, K., Charitsi, A., and Merminod, B., 2018. Icy lakes extraction and water-ice classification using Landsat 8 OLI multispectral data. *International Journal of Remote Sensing*, **39** (11): 3646-3678.

Chen, Y., and Gong, Y. C., 2010. A method for optical remote sensing image ship extraction in cloudy sea background. *Opto-Electronic Engineering*, **37** (12): 103-109.

Cui, Z. Y., Li, Q., Cao, Z., and Liu, N. Y., 2019. Dense attention pyramid networks for multi-scale ship detection in SAR images. *IEEE Transactions on Geoscience and Remote Sensing*, **57** (11): 8983-8997.

Fang, L., Wei, X., Yao, W., Xu, Y. S., and Stilla, U., 2017. Discriminative features based on two layers sparse learning for glacier area classification using SAR intensity imagery. *IEEE Journal of Selected Topics in Applied Earth Observations and Remote Sensing*, **10** (7): 3200-3212.

Han, H., Im, J., and Kim, H., 2016. Variations in ice velocities of pine island glacier ice shelf evaluated using multispectral image matching of Landsat time series data. *Remote Sensing of Environment*, **186**: 358-371.

Han, Y. L., Li, P., Zhang, Y., Hong, Z. H., and Wang, Z., 2018. Combining active learning and transductive support vector machines for sea ice detection. *Journal of Applied Remote Sensing*, **12** (2): 026016.

Heiselberg, H., 2019. Aircraft and ship velocity determination in sentinel-2 multispectral images. *Sensors*, **19** (13): 2873.

Heiselberg, H., 2020. Ship-iceberg classification in SAR and multispectral satellite images with neural networks. *Remote Sensing*, **12** (15): 2353.

Heiselberg, P., and Heiselberg, H., 2017. Ship-Iceberg discrimination in Sentinel-2 multispectral imagery by supervised classification. *Remote Sensing*, **9** (11): 1156.

Herzfeld, U. C., Williams, S., Heinrichs, J., Maslanik, J., and Sucht, S., 2016. Geostatistical and statistical classification of sea-ice properties and provinces from SAR data. *Remote Sensing*, **8** (8): 616.

Hwang, J. I., and Jung, H. S., 2018. Automatic ship detection using the artificial neural network and support vector machine from X-Band SAR satellite images. *Remote Sensing*, **10** (11): 1799.

Hwang, J. I., Chae, S. H., Kim, D., and Jung, H. S., 2017. Application of artificial neural networks to ship detection from X-Band Kompsat-5 imagery. *Applied Sciences*, **7** (9): 961.

Iervolino, P., and Guida, R., 2017. A novel ship detector based on the generalized-likelihood ratio test for SAR imagery. *IEEE Journal of Selected Topics in Applied Earth Observations and Remote Sensing*, **10** (8): 3616-3630.

Ji, C., Yang, X. D., and Chen, C. Q., 2017. Target region locating algorithm for ship visual image under sea-sky background. *Fire Control & Command Control*, **42** (7): 66-71.

Johansson, M., Espeseth, M., Brekke, C., and Holtet, B., 2020. Can mineral oil slicks be distinguished from newly formed sea ice using synthetic aperture radar? *IEEE Journal of Selected Topics in Applied Earth Observations and Remote Sensing*, **13**: 4996-5010.

Liu, G., Li, L., Gong, H., Jin, Q. W., Li, X. W., Song, R., *et al.*, 2017. Multisource remote sensing imagery fusion scheme based on Bidimensional Empirical Mode Decomposition (BEMD) and its application to the extraction of bamboo forest. *Remote Sensing*, **9** (1): 19.

Lohse, J., Doulgeris, A. P., and Dierking, W., 2019. An optimal decision-tree design strategy and its application to sea ice classification from SAR imagery. *Remote Sensing*, **11** (13): 1574.

MacGregor, J. A., Fahnestock, M. A., Colgan, W. T., Larsen, N. K., and Welker, J. M., 2020. The age of surface-exposed ice along the northern margin of the Greenland ice sheet. *Journal of Glaciology*, **66** (258): 667-684.

Mattyus, G., 2013. Near real-time automatic marine vessel detection on optical satellite images. *International Archives of the Photogrammetry, Remote Sensing and Spatial Information Sciences*, **40** (1): 233-237.

Miguel, M., Flavio, P., Corrado, F., and Lorenzo, G., 2017. Synthetic aperture radar analysis of floating ice at Terra Nova Bay−An application to ice eddy parameter extraction. *Journal of Applied Remote Sensing*, **11** (2): 026041.

Nie, T., He, B., Bi, G., Zhang, Y., and Wang, W. S., 2017. A method of ship detection under complex background. *ISPRS International Journal of Geo-Information*, **6** (6): 159.

Park, J. W., Korosov, A. A., Babiker, M., Won, J. S., and Kim, H. C., 2020. Classification of sea ice types in Sentinel-1 synthetic aperture radar images. *The Cryosphere*, **14** (8): 2629-2645.

Park, K. A., Park, J. J., Jang, J. C., Lee, J. H., Oh, S., and Lee, M., 2018. Multi-spectral ship detection using optical, hyperspectral, and microwave SAR remote sensing data in coastal regions. *Sustainability*, **10** (11): 1-23.

Ren, X. Y., 2016. Research on in-shore ship detection fromoptical remote sensing image *via* auxiliary knowledge. Master thesis. National University of Defense Technology.

Ressel, R., and Singha, S., 2016. Comparing near coincident space borne C and X band fully polarimetric SAR data for Arctic sea ice classification. *Remote Sensing*, **8** (3): 198.

Ressel, R., Singha, S., Lehner, S., Rsel, A., and Spreen, G., 2016. Investigation into different polarimetric features for sea ice classification using X-band synthetic aperture radar. *IEEE Journal of Selected Topics in Applied Earth Observations and Remote Sensing*, **9** (7): 3131-3143.

Shah, E., Jayaprasad, P., and James, M. E., 2019. Image fusion of SAR and optical images for identifying Antarctic ice features. *Journal of the Indian Society of Remote Sensing*, **47** (12): 2113-2127.

Su, H., Ji, B., and Wang, Y., 2019. Sea ice extent detection in the Bohai Sea using Sentinel-3 OLCI data. *Remote Sensing*, **11** (20): 2436.

Sukawattanavijit, C., Chen, J., and Zhang, H., 2017. GA-SVM algorithm for improving land-cover classification using SAR and optical remote sensing data. *IEEE Geoscience and Remote Sensing Letters*, **14** (3): 284-288.

Vijay, K., and Gopalan, V., 2012. High resolution TerraSAR-X image speckle suppression and its fusion with multispectral

IRS LISS-III data for Himalayan glacier feature extraction. *Journal of the Indian Society of Remote Sensing*, **40** (2): 325-334.

Wang, B. Y., Zhang, R., Yuan, Y., and Yin, D., 2011. A new multi-level threshold segmentation method for ship targets detection in optical remote sensing images. *Journal of University of Science and Technology of China*, **41** (4): 293-298 (in Chinese with English abstract).

Xie, T., Perrie, W., Wei, C., and Zhao, L., 2020. Discrimination of open water from sea ice in the Labrador sea using quad-polarized synthetic aperture radar. *Remote Sensing of Environment*, **247**: 111948.

Yu, Z., Wang, T. W., Zhang, X., Zhang, Z., and Ren, P., 2019. Locality preserving fusion of multi-source images for sea-ice classification. *Acta Oceanologica Sinica*, **38** (7): 129-136.

Zhu, C. R., Zhou, H., Wang, R. S., and Guo, J., 2010. A novel hierarchical method of ship detection from spaceborne optical image based on shape and texture features. *IEEE Transactions on Geoscience and Remote Sensing*, **48** (9): 3446-3456.

(Edited by Chen Wenwen)